Strong configuration-interaction contributions to the angle-resolved 4*p* photoelectron spectra of atomic xenon

S. Kosugi,[1,2] F. Koike,[2] M. Iizawa,[3] F. Hosseini,[4,5] J. Martins,[4,6] T. Marchenko,[4] O. Travnikova,[4] J. D. Bozek,[5] K. Ito,[5] S. Fritzsche,[7,8,9] M. N. Piancastelli,[4] M. Simon,[4] and Y. Azuma[2,10,*]

[1]*Department of Physics, Tokyo Gakugei University, Tokyo 184–8501, Japan*
[2]*Department of Materials and Life Sciences, Sophia University, Tokyo 102–8554, Japan*
[3]*Department of Physics, Rikkyo University, Tokyo 171–8501, Japan*
[4]*Sorbonne Université, CNRS, UMR 7614, Laboratoire de Chimie Physique-Matière et Rayonnement, F-75005 Paris, France*
[5]*Synchrotron SOLEIL, L'Orme des Merisiers, Saint-Aubin, BP 48, F-91192 Gif-sur-Yvette Cedex, France*
[6]*X-ray Science Division, Advanced Photon Source, Argonne National Laboratory, Lemont, Illinois 60439, USA*
[7]*Helmholtz-Institut Jena, Fröbelstieg 3, D-07743 Jena, Germany*
[8]*GSI Helmholtzzentrum für Schwerionenforschung GmbH, D-64291 Darmstadt, Germany*
[9]*Theoretisch-Physikalisches Institut, Friedrich-Schiller-Universität Jena, Max-Wien-Platz 1, D-07743 Jena, Germany*
[10]*Department of Physics, Indian Institute of Technology Delhi, Hauz Khas, New Delhi 110016, India*

(Received 3 October 2022; revised 13 February 2023; accepted 13 February 2023; published 28 February 2023)

High-resolution photoelectron spectra of xenon (Xe) were measured in the 4*p* photoionization region. The anisotropy parameters β were obtained for several photoelectron peaks with angle-resolved photoelectron measurements. The various complicated spectral features were observed due to the perturbed $4p^{-1}$ spin-orbit doublet and adjacent satellite structures. An analysis based on a relativistic multiconfiguration calculation has been carried out. The key role of the strong interactions between the $4p^{-1}$ core hole and the $4d^{-2}nl$ configurations has been investigated in detail. Experimental peak energies and intensities are in good agreement with theory. We find that the many of the complicated features are $4d^{-2}nl$ satellite lines, and their intensities are determined mostly by the amount of $4p^{-1}$ configurations that are mixed in. The experimental β values agree quite well with theory, indicating that the photoelectron angular distributions are also strongly influenced by the 4*p* direct-ionization contributions.

DOI: 10.1103/PhysRevA.107.022814

I. INTRODUCTION

The photoelectron spectra of various atomic-shell ionization may show electron correlation effects. In these spectra, it is possible to observe several satellite lines in addition to the main photoelectron peaks originating from strong interactions with the inner-shell vacancy state and other states. Such structures were observed in the photoelectron spectra obtained by inner-shell photoionization of various rare gases including Ne 2*s* [1–4], Ar 3*s* [1–5], Kr 4*s* [1–3,6–8], Kr 3*p* [1,9–11], and Xe 5*s* [1–3,7,8]. Furthermore, Hikosaka and Fritzsche [12] have recently reported Coster-Kronig (CK) and super Coster-Kronig (SCK) transitions from the Xe 4*s* core-hole state. In the present paper, we report on the Xe 4*p* photoelectron spectrum. As pointed out by earlier authors [13,14], the appearance of the $4p^{-1}$ spectrum is significantly different from the usual dual peak of the $4p_{1/2}$ and $4p_{3/2}$ fine-structure doublet. The Xe 4*p* photoelectron spectrum exhibits quite complicated structures caused by strong correlation contributions. Svensson *et al.* [10] observed the spectrum for the first time and confirmed that the $4p_{1/2}$ component was missing and that some broadly spread features were seen instead. Wendin and Ohno [15] explained that the $4p_{1/2}{}^{-1}$ state became washed out due to $4p_{1/2}{}^{-1} \rightarrow 4d^{-2}\varepsilon f$ SCK transitions, based on their many-body perturbation calculation. Heinäsmäki *et al.* [16] performed a multiconfiguration Dirac-Fock (MCDF) calculation. Hikosaka *et al.* [17,18] studied the Auger decay of Xe^+ states following 4*p* ionization with a multielectron coincidence method.

Nevertheless, the previous measurements and theory fell short of providing satisfactory explanation. Furthermore, no experimental or theoretical work on angular correlations of photoelectrons was reported.

In this work, features due to strong configuration interactions in the Xe 4*p* inner subshells have been observed and clearly identified by high-resolution photoelectron spectroscopy. Binding energies obtained by MCDF calculations and detailed assignments are reported. The calculated photoionization cross sections and Auger rates of each state agreed well with the experimental spectrum. The anisotropy parameters β have been obtained by angle-resolved measurements. Our theoretical calculations agree reasonably well within the uncertainty of the experimental β values.

We briefly describe the experiment in the next section. In Sec. III, we discuss the details of our theoretical calculation procedure. In Sec. IV, we compare and discuss the compari-

*y-azuma@sophia.ac.jp

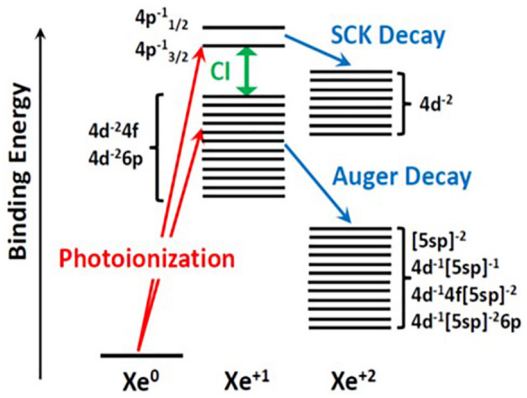

FIG. 1. Schematic energy level diagram for Xe $4p$ photoionization and the following Auger (CK, or SCK) decay.

son of our experimental results and calculations. Finally, we give some concluding remarks in Sec. V.

II. EXPERIMENT

The measurements were performed at the PLEIADES beamline of the 2.75-GeV French national synchrotron facility SOLEIL. The PLEIADES beamline is equipped with the HU80 undulator, delivering variable polarization in the energy range between 15 and 900 eV, and a high-resolution monochromator employing varied groove-depth and varied line-spacing gratings. Kinetic energies of the emitted electrons were measured by a hemispherical electron-energy analyzer (VG Scienta R4000) mounted perpendicular to the propagation axis of the photon beam. The analyzer was used with a constant pass energy of 10 eV, resulting in a total experimental resolution of about 120 meV at 664.90-eV photon energy. The calibration of the angle dependence of the efficiency of the analyzer was accomplished by Ne $2p$ photoelectron measurements. The measured Ne $2p$ intensities were normalized using the angular anisotropy parameters β from a previous reference [19]. The photon energy and the ejected electron energy were calibrated by the Xe $5p$ photoelectron [20] and Xe *NOO* Auger lines [21]. All of the photoelectron spectra were normalized with respect to the gas pressure, acquisition time, and photon flux, monitored continuously during the measurements. Anisotropy parameters β were determined by obtaining the peak-intensity ratio for parallel and perpendicular directions to the photon polarization, where the peaks were fitted by the Voigt function.

III. THEORY

We performed a series of MCDF calculations [22]. Figure 1 illustrates a schematic energy level diagram Xe $4p$ photoionization and the subsequent nonradiative decay processes. As pointed out by Heinäsmäki *et al.* [16], the $4p^{-1}$ single-hole levels are strongly mixed with those from the $4d^{-2}4f$ and other $4d^{-2}$ double-hole configurations such as $4d^{-2}6p$ by configuration interaction (CI). The $4p^{-1}$ hole states mostly decay into the $4d^{-2}$ double-hole states by fast SCK transitions with lifetime widths so large that they are not discernible as peaks [16], whereas the $4d^{-2}4f$, and $4d^{-2}6p$ mostly decay into $[5sp]^{-2}$, $4d^{-1}[5sp]^{-1}$, $4d^{-1}4f[5sp]^{-2}$, or $4d^{-1}[5sp]^{-2}6p$ by CK or Auger transitions. Here, $[5sp]^{-q}(q = 1, 2)$ indicates that one or two electrons are removed from $5s$ and/or $5p$ subshells. However, due to the CI in the upper levels, these nonradiative decay processes are modified significantly, as discussed in detail in the rest of the present paper.

For the energy-level calculations, we employed GRASP92, a general-purpose relativistic atomic structure program from the GRASP family [23] with some modifications and a code package for relativistic atomic transition, ionization, and recombination properties (RATIP) [24,25], which works independently of GRASP but requires the GRASP wave functions. We also used the RATIP programs for photoionization dynamics and nonradiative as well as radiative decay processes.

It has been found most crucial that we correctly evaluate the configuration mixing of $4p^{-1}$ with their adjacent states. For the singly ionized Xe^+ excited states, we constructed the set of wave functions stepwise in the following manner. First, we performed the MCDF optimization procedure for $4p^{-1}$ with the total angular momentum $J = 1/2, 3/2$ configurations. In the second step, we included $4d^{-2}4f$ $J = 1/2, 3/2$ configurations and performed the MCDF optimization procedure for the $4f$, $5s$, and $5p$ orbitals whereas the other orbitals were kept fixed. Here, 22 configuration-state functions were simultaneously optimized. Then, $5f$, $6f$, and $6p$ orbitals were included one by one in this order and the MCDF optimization was performed with the inclusion of each new orbital while the others were fixed. The number of many-electron multiconfiguration wave functions, i.e., atomic-state functions (ASFs) that were subject to the simultaneous optimization were 40, 60, and 80, respectively, for the stepwise inclusion of $5f$, $6f$, and $6p$ atomic orbitals. For the initial state of the photoionization of the Xe^0 ground state, we considered the correlation contributions of $4f$ orbitals by including the $4f^2\,5s^2\,5p^4$ configurations in the MCDF optimization of the $5s^2\,5p^6$ ground state.

The binding energies for the photoionization process can be calculated by subtracting the Xe^0 ground-state energy from the Xe^+ excited-state energies. To highlight the major configuration-interaction features, Table I lists the binding energies of the lowest-four and the highest-two levels for the simplest case with only $4p^{-1}$ and $4d^{-2}4f$ as the Xe^+ $J = 1/2$, $3/2$ excited-state configurations. The percentage fractions of configuration admixture are also listed. Although the contributions of the other configurations may also be appreciable, we will discuss them later in this paper when we compare the theory with the experimental results. The calculated photoionization cross sections and the anisotropy parameters β for this simplest case are listed for reference.

We find in Table I that the $4p^{-1}$ diagram states (states no. 21 and no. 22) contain substantial mixtures of $4d^{-2}4f$ configurations. This results in calculated binding energies of 177.75 and 170.94 eV for $J = 1/2$ and $3/2$, respectively, shifted considerably compared to calculation results obtained without the $4d^{-2}4f$ configuration interactions (169.21 and 156.82 eV for $J = 1/2$ and $3/2$, respectively). In addition, we find in Table I that the $4d^{-2}4f$ states (states no. 1 to no. 4) also have considerable amounts of $4p^{-1}$ contribution. The

TABLE I. Calculated binding energies, photoionization cross sections, and anisotropy parameter βs of the lowest-four and the highest-two levels for the simplest case with only $4p^{-1}$ and $4d^{-2}4f$ as the Xe^+ $J = 1/2, 3/2$ excited-state configurations. Percentage fractions of configuration admixture are also given.

State No.	Angular momentum J	Binding energy (eV)	Configuration admixture $4p^{-1}$ (%)	Configuration admixture $4d^{-2}4f$(%)	Cross section (10^{-3} a.u.)	Anisotropy parameter β
1	3/2	145.68	25.73	74.27	1.256	1.484
2	3/2	146.32	15.22	84.78	0.729	1.486
3	1/2	146.48	0.00	100.00	0.007	1.515
4	3/2	147.19	4.56	95.45	0.218	1.487
21	3/2	170.94	43.17	56.83	2.209	1.463
22	1/2	177.75	67.49	32.51	1.521	1.483

photoionization intensities of the $4d^{-2}4f$ states are due to intensity borrowing from $4p^{-1}$.

The Xe $4p$ photoelectron spectra have been calculated using the RATIP program [25] which supports different and not quite orthogonal sets of orbitals for the initial and final bound states. The distorted waves with a static exchange continuum wave function (partial wave of the outgoing electron) were generated in the program [26]. We calculated the photoionization process for 665.00-eV linearly polarized incident photon in length form (Babushkin gauge) and also in velocity form (Coulomb gauge). For these two gauges, the results differed by less than 6% in all of the calculated photoionization cross sections except the $4p^{-1}$ diagram lines. The corresponding differences for ${4p_{1/2}}^{-1}$ and ${4p_{3/2}}^{-1}$ diagram lines were, respectively, 14 and 16%, which are larger than others because the MCDF optimization was mainly focused on the satellite levels. The mean values between those forms are used below to display and compare the theoretical results with experiment. We also calculated the anisotropy parameters β for linearly polarized incident light. Again, these β parameters were generated with both length and velocity forms and found to differ by less than 0.2% for all of the photoionization peaks considered. In total, 80 spectral lines were calculated.

The Xe^+ ionic excited states undergo radiative or nonradiative decays into the lower lying states. The lifetimes of the excited states are reflected in the spectral linewidths. To obtain the lifetime widths, we calculated the rates of both optical and Auger (CK or SCK) transitions. For the final-state wave functions, we used the set of electron orbitals that were obtained for the Xe^+ ionic excited states; we generated the ASFs and the state energies by means of the CI calculations.

For the optical transitions, we used the RATIP program. The radiative lifetime widths obtained were mostly on the order of 10^{-3} eV or less, ignorable for the present analysis.

For the Auger (CK or SCK) transitions, we used the RATIP program. The mean radii of the $5f$ and $6f$ atomic orbitals turned out to be quite large, $10.3\,a_0$ for $5f$ and $17.6\ a_0$ for $6f$, where a_0 is the Bohr radius. So, we considered only the $4d^{-2}4f$ and $4d^{-2}6p$ configurations in the initial Xe^+ ionic excited states. We have therefore included 40 ASFs in the system before the decay. For the final states of the decay processes, we considered the states with the $4d^{-2}$, $4d^{-1}5sp^{-1}$, $4d^{-1}4f5sp^{-2}$, $4d^{-1}5sp^{-2}6p$, and $5sp^{-2}$ configurations, where $5sp^{-q}$ indicates that $q = 1$ or2 electrons are removed from the $5s$ and/or $5p$ subshell. The total number of the ASFs included was 850. For the lower-lying $4d^{-2}4f$ and $4d^{-2}6p$ states below the $Xe^{+2}4d^{-2}$ threshold, we excluded the $4d^{-2}$ configurations from the Auger (CK or SCK) calculation. We considered the possible transitions from the 40 excited states to the lower 850 states for these spectra; we have 33 639 transitions that consumed about 12 days of computational time on a desktop server. The calculated lifetime widths of the states below the $Xe^{+2}4d^{-2}$ threshold are presented in Table II. Above the $Xe^{+2}4d^{-2}$ threshold, the calculated lifetime widths are quite large and smear out the spectral lines. In fact, the SCK widths that are evaluated within the minimal basis states, i.e., without the influence of the $4d^{-2}4f$ and $4d^{-2}6p$ configurations are 33.7 eV for $4p^{-1}{}^2P_{1/2}$, and 15.8 eV for $4p^{-1}{}^2P_{3/2}$, respectively. In the $4d^{-2}4f$ and $4d^{-2}6p$ configurations above the $Xe^{+2}4d^{-2}$ threshold, there might be some effects from core-quenching ionizations which could further broaden their lifetime widths.

IV. RESULTS AND DISCUSSION

Figure 2 shows the photoelectron spectra following Xe $4p$ photoionization by 664.90-eV incident photons. We have chosen the photon energy that is sufficiently higher than the $4p$ ionization threshold (by about 172 eV; see Table II). Therefore, no peak shift or deformation due to postcollision-interaction (PCI) effects have to be taken into account [27]. The spectra were measured at the angles of 0° and 90° with respect to the electric vector of the linearly polarized photon beam. The observed intensities are denoted as $I(0^\circ)$ and $I(90^\circ)$, respectively. For comparison with theory, Fig. 2 also plots $I(0^\circ) + 2I(90^\circ)$, which is equivalent to the total cross section. The corresponding assignments and binding energies are presented in Table II. The vertical bars are the cross sections obtained from our calculation. The dashed curve is the theoretical spectrum obtained from the convolution of the theoretical cross sections with a Voigt function. The Lorentzian profile with full width at half maximum corresponding to the calculated lifetime width was used for convolution for all the peaks below 154 eV. Gaussian contribution of 120 meV was incorporated to account for the instrumental width. The vertical scales for the experimental and theoretical spectra were normalized with regard to peak A. There are other relatively large theoretical peaks in the

TABLE II. Binding energies, relative intensities, lifetime widths, anisotropy parameter βs, and dominant configurations of the main states contributing to the observed features.

	Binding energy exp. (eV)	Binding energy theory (eV)	Relative intensity exp.	Relative intensity theory	Lifetime width exp. (eV)	Lifetime width theory (eV)	Anisotropy parameter β exp.	Anisotropy parameter β theory	Dominant configuration admixtures (in %)							
A	145.53 ± 0.01	145.59	1.00 ± 0.03	1.00	0.54 ± 0.02	0.499	1.45 ± 0.04	1.485	68.3	$4d^8\,4f$	29.5	$4p^5(^2P_{3/2})$				
B	146.28 ± 0.01	146.27	0.22 ± 0.02	0.38	0.23 ± 0.03	0.234	1.42 ± 0.06	1.500	76.0	$4d^8\,4f$	11.3	$4p^5(^2P_{3/2})$	2.5	$4d^8\,6p$		
		146.31		0.04		0.273		1.487	94.5	$4d^8\,6p$	1.3	$4p^5(^2P_{3/2})$	1.1	$4d^8\,4f$		
C	147.07 ± 0.03	147.13	0.10 ± 0.02	0.12	0.27 ± 0.10	0.298	1.37 ± 0.12	1.487	92.5	$4d^8\,4f$	3.7	$4p^5(^2P_{3/2})$				
D	148.29 ± 0.05	148.32	0.07 ± 0.01	0.01	0.37 ± 0.13	0.013	1.3 ± 0.2	1.493	72.6	$4d^8\,5f$	21.1	$4d^8\,4f$				
		148.42		0.02		0.118		1.520	80.5	$4d^8\,5f$	14.3	$4d^8\,4f$	1.1	$4p^5(^2P_{1/2})$		
		148.47		0.01		1.185		1.492	83.2	$4d^8\,5f$	10.8	$4d^8\,4f$				
E	148.88 ± 0.03	148.80	0.07 ± 0.01	0.03	0.21 ± 0.08	0.042	1.2 ± 0.3	1.515	62.2	$4d^8\,4f$	15.8	$4d^8\,6p$	12.5	$4d^8\,5f$		
		149.05		0.07		0.021		1.493	35.8	$4d^8\,4f$	29.6	$4d^8\,6p$	9.3	$4d^8\,5f$		
		149.14		0.03		0.016		1.494	61.6	$4d^8\,6p$	27.7	$4d^8\,4f$				
F	150.37 ± 0.05	150.27		0.02		0.236		1.519	91.4	$4d^8\,5f$	3.3	$4d^8\,4f$				
G	151.87 ± 0.03	152.17		0.03				1.493	64.2	$4d^8\,5f$	22.5	$4d^8\,4f$				
		154.64		0.15				1.510	34.1	$4d^8\,4f$	33.5	$4d^8\,6f$	17.7	$4d^8\,5f$	1.0	$4p^5(^2P_{1/2})$
		155.02		0.08				1.514	86.2	$4d^8\,6f$	6.7	$4d^8\,4f$	5.4	$4p^5(^2P_{1/2})$		
		155.17		0.06				1.514	76.9	$4d^8\,6f$	14.5	$4d^8\,4f$	4.0	$4p^5(^2P_{1/2})$		
		172.06		1.47				1.463	53.1	$4d^8\,4f$	41.1	$4p^5(^2P_{3/2})$	3.6	$4d^8\,5f$	1.8	$4d^8\,6f$
		178.70		1.00				1.483	64.6	$4p^5(^2P_{1/2})$	31.6	$4d^8\,4f$	2.5	$4d^8\,5f$	1.3	$4d^8\,6f$

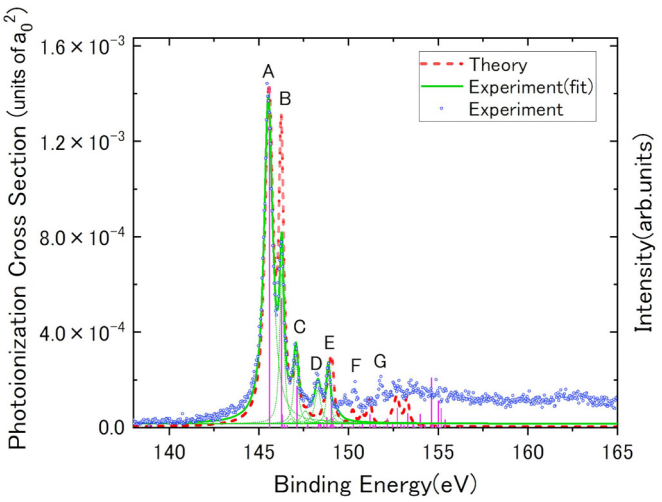

FIG. 2. Photoelectron spectrum above the Xe $4p$ ionization threshold excited by 664.90-eV photons. The data points represent $I(0°) + 2I(90°)$, which correspond to the angle-integrated total intensity (see text). Solid curve through the data points represents the fit result. The corresponding assignments and binding energies are presented in Table II. Vertical bars are photoionization cross sections obtained from our calculation at the photon energy of 665.00 eV. Dashed curve is the theoretical spectrum obtained from convolution of the cross sections with the calculated core-hole lifetime widths and experimental resolution.

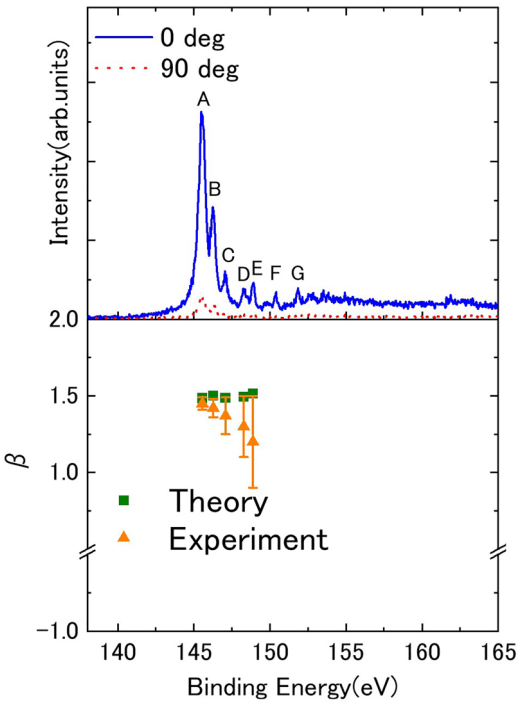

FIG. 3. (Upper) Photoelectron spectrum around the Xe $4p$ ionization threshold with 664.90-eV photons measured at two emission angles, 0° (solid curve) and 90° (dotted curve). (Lower) Experimental values of the β parameter for some of the peaks observed in the upper part of the figure. Results of theoretical calculations are also shown in the figure.

area near 155-eV binding energy that do not appear in the experimental results. We will discuss this point in the following paragraph.

The experimental and theoretical binding energies, theoretical cross sections, and theoretical lifetime widths are listed in Table II. The most prominent peaks are A and B. The configuration fractions for peak A are 68.3% from $4d^{-2}4f$ and 29.5% from $4p^5(^2P_{3/2})$ configurations. Peak B consists of 76.0% from $4d^{-2}4f$ and 11.3% from $4p^5(^2P_{3/2})$ configurations. In those two peaks, the $4d^{-2}4f$ configurations are dominant compared to $4p^5(^2P_{3/2})$. Considering these facts and the fairly good agreement between the theory and experiment as seen in Fig. 2, we can assign the peaks A and B as identified by the dominant $4d^{-2}4f$ configuration. However, we must note that the photoionization intensities of A and B originate from the smaller $4p^{-1}$ configuration component mixed in them. In fact, the $4p^5(^2P_{3/2})$ diagram line photoionization cross section calculated with single configuration without the contribution of $4d^{-2}4f$ or any other configurations is 5.00×10^{-3}a.u. The cross sections of peaks A and B are 1.437×10^{-3} a.u. and 0.545×10^{-3} a.u., which correspond to 28.7 and 10.9% of 5.00×10^{-3} a.u., respectively. They almost coincide with the percentage fractions 29.5 and 11.3% for $4p^{-1}$ configurations mixed in A and B. In previous works [15,16], it was pointed out that no photoelectron line of $4p_{1/2}$ was seen due to the very fast SCK decay process from the $4d$ hole state. This same argument should also apply to the $4p_{3/2}$ photoelectron line. As shown in Table II, the contribution of the $4p^5(^2P_{3/2})$ configuration is 41.1% to the level at 172.06 eV, and $4p^5(^2P_{1/2})$ contributes 64.6% to the level at 178.70 eV. These peaks are in fact about 30 eV away from the peaks A and B that contain $4p^5(^2P_{3/2})$ configurations. It is natural to expect that the $4p^5(^2P_{3/2})$ level at 172.06 eV is dispersed into the background continuum due to the fast SCK decay. In Fig. 2, a strong rise in the experimental cross-section curve can be observed at binding energies around 150 eV and higher. This can be considered as part of the tails of SCK decay of the two highest $4p^5(^2P_{3/2})$ and $4p^5(^2P_{1/2})$ states. Another notable feature of this comparison is that there is no peak in the experimental spectrum near the binding energy of 155 eV in Fig 2, despite the presence of theoretical peaks. As seen from the level diagram in Fig. 1, the $Xe^{+1}4p^{-1}$ states are energetically above the $Xe^{2+}4d^{-2}$ double-hole states. The theoretically evaluated threshold energy is slightly higher than 155 eV, giving rise to the discrete spectral peaks around 155 eV. However, the actual threshold might be somewhat lower. Above the threshold, even an autoionization of $4f$ or np electrons may occur owing to the rearrangement (recoupling) of the two $4d$ holes (valence-multiplet Auger decay [28–30]). Therefore, the theoretical peaks around 155 eV disperse as continua in the experimental spectrum.

We have also measured the values of the anisotropy parameter β by comparing the spectral intensities for photoelectrons detected parallel to and perpendicular to the incident photon linear polarization. In Table II and Fig. 3, the experimental β parameters are shown, together with the results of theoretical calculations. The observed anisotropy parameter β values scatter between approximately 1.1 and 1.5. The observed β values of the prominent peaks A, B, and C are 1.45 ±

0.04, 1.42 ± 0.06, and 1.37 ± 0.12, respectively, in good agreement with the corresponding theoretical values 1.49, 1.50, and 1.49, within the experimental uncertainty. Figure 3 also shows the observed β of the higher binding-energy peaks D and E. Their β values are somewhat lower than the theoretical results. This may be due to the fact that the spectrum at 90° is weak and the contribution from the background SCK decay could not be well separated. Although within the experimental uncertainties, the experimental β has clear binding-energy dependence whereas the theory remains constant. This might give a challenge to the future theoretical work. Still, the overall agreement between the theory and experiment is reasonably good. We also note that the β parameters for $4p^5(^2P_{1/2})$ state at 178.70-eV binding energy and $4p^5(^2P_{3/2})$ state at 172.06-eV binding energy were calculated to be 1.48 and 1.46, respectively as given in Table II, even though those two peaks are dispersed and could not be observed experimentally. Those values are more or less the same in magnitude to the β parameters of the experimentally observed peaks, that are assigned as the $4d^{-2}nf$ and $4d^{-2}np$ states. This suggests the excitations of those states are determined by the $4p$ direct ionization contributions through some mixing of the $4p^{-1}$ configurations.

In the present paper, we have argued that the usually prominent $4p^5(^2P_{1/2})$ and $4p^5(^2P_{3/2})$, diagram lines do not make distinct appearance in the photoelectron spectra due to their strong coupling with the doubly ionized $4d^{-2}$ states. Instead of appearing as observable peaks, they form a broad continuum as seen in the experimental spectra above 150-eV binding energy in Fig. 2. One may argue that the singly ionized $4p^5(^2P_{1/2})$ and $4p^5(^2P_{3/2})$ diagram states cannot be the intermediate states for the decay to the doubly ionized $4d^{-2}$ states due to their strong couplings, and that we must treat the double-ionization processes as collective effects of many electrons. Instead, we assume that the $4p^{-1}$ configuration is one of the constituents of the intermediate states. The modification of the electron orbital functions due to the interactions between the $4p^{-1}$, $4d^{-2}nf$, and $4d^{-2}np$ configurations in the intermediate states are considered within the scheme of MCDF optimization. The agreement between the theory and experiment for several discrete spectral lines as seen in Fig. 2 suggests that the $4p^{-1}$ configuration plays an important role in describing the intermediate states of the two-step double ionization.

V. CONCLUSION

Measurements of the photoelectron spectrum over the Xe $4p$ ionization region were carried out with a high-resolution hemispherical electron analyzer using synchrotron radiation. We determined several spectral peaks A to G (see Table II and Fig. 2) arising from the $4d^{-2}nl$ states. The binding energies and widths of the spectral peaks were obtained and assigned according to the MCDF wave functions. The calculated photoionization cross sections of each state reproduced the intensity distribution of the experimental spectrum quite well. It was found that the main peaks A at 145.53-eV and B at 146.28-eV binding energy should be assigned as $4d^{-2}4f$, while the diagram $4p^{-1}(^2P_{3/2})$ state is dissolved into the continuum and contributes to higher binding energies. It was also found that the valence-multiplet Auger decay process plays an important role for the nonradiative decay following the Xe $4p$ photoionization around 155-eV binding energy and higher, giving the continuum background spectral structure.

We measured the angle dependence of the spectral intensities and obtained the anisotropy parameter β values for the spectral lines A to E (see Table II and Fig. 3). Our theoretical calculations agree reasonably well within the uncertainty of the experimental β values. The values of β were found to be dominated by the $4p$ direct-ionization contributions throughout the peaks considered. In the present study, we clearly resolved the spectral lines by using the apparatus with improved resolution and identified the correlation satellites A to G as listed in Table II. The MCDF calculation with extended number of basis wave functions and atomic states enabled us to determine the electron configurations for the assigned levels A to G. The angle-resolved photoelectron spectroscopy measurement enabled us to investigate the role of the diagram $4p^{-1}$ states on the excitation of the satellite levels.

ACKNOWLEDGMENTS

This material is based on work supported by the Japan Society for the Promotion of Science through Grants-in-Aid for Scientific Research Category "C," Grants No. 23600009 and No. 17K05600. The authors are grateful to the SOLEIL staff for operating the facility and providing beamtime under Project No. 20191638.

[1] S. Svensson, B. Eriksson, N. Mårtensson, G. Wendin, and U. Gelius, J. Electron Spectrosc. Relat. Phenom. **47**, 327 (1988).

[2] M. O. Krause, S. B. Whitfield, C. D. Caldwell, J. Z. Wu, P. van der Meulen, C. A. de Lange, and R. W. C. Hansen, J. Electron Spectrosc. Relat. Phenom. **58**, 79 (1992).

[3] A. Kikas, S. J. Osborne, A. Ausmees, S. Svensson, O. P. Sairanen, and S. Aksela, J. Electron Spectrosc. Relat. Phenom. **77**, 241 (1996).

[4] U. Becker and D. Shirley, Phys. Scr., T **31**, 56 (1990).

[5] U. Becker, B. Langer, H. G. Kerkhoff, M. Kupsch, D. Szostak, R. Wehlitz, P. A. Heimann, S. H. Liu, D. W. Lindle, T. A. Ferrett, and D. A. Shirley, Phys. Rev. Lett. **60**, 1490 (1988).

[6] N. Berrah, A. Farhat, B. Langer, B. M. Lagutin, Ph. V. Demekhin, I. D. Petrov, V. L. Sukhorukov, R. Wehlitz, S. B. Whitfield, J. Viefhaus, and U. Becker, Phys. Rev. A **56**, 4545 (1997).

[7] S. Alitalo, A. Kivimäki, T. Matila, K. Vaarala, H. Aksela, and S. Aksela, J. Electron Spectrosc. Relat. Phenom. **114**, 141 (2001).

[8] A. Caló, S. Sankari, A. Kivimäki, H. Aksela, and S. Aksela, J. Phys. B **39**, 4169 (2006).

[9] S. Kosugi, F. Koike, T. Nagayasu, F. Hosseini, J. Martins, T. Marchenko, O. Travnikova, M. Oura, T. Gejo, J. R. Harries, J. D. Bozek, K. Ito, E. Sokell, S. Fritzsche, M. N. Piancastelli, M. Simon, and Y. Azuma, Phys. Rev. A **101**, 042505 (2020).

[10] S. Svensson, N. Mårtensson, E. Basilier, P. A. Malmquist, U. Gelius, and K. Siegbahn, Phys. Scr. **14**, 141 (1976).
[11] M. Ohno and G. Wendin, Phys. Scr. **16**, 299 (1977).
[12] Y. Hikosaka and S. Fritzsche, Phys. Chem. Chem. Phys **24**, 17535 (2022).
[13] P. Lukirskii, T. M. Zimkina, and I. A. Brytov, Izv. Akad. Nauk SSSR, Ser. Fiz. **28**, 772 (1964) [Bull. Acad. Sci. USSR Phys. Ser. **28**, 681 (1964)].
[14] K. Codling and R. P. Madden, Appl. Opt. **4**, 1431 1965).
[15] G. Wendin and M. Ohno, Phys. Scr. **14**, 148 (1976).
[16] S. Heinäsmäki, H. Aksela, J. Nikkinen, E. Kukk, A. Kivimäki, S. Aksela, and S. Fritzsche, J. Electron Spectrosc. Relat. Phenom. **137**, 281 (2004).
[17] Y. Hikosaka, P. Lablanquie, F. Penent, T. Kaneyasu, E. Shigemasa, J. H. D. Eland, T. Aoto, and K. Ito, Phys. Rev. Lett. **98**, 183002 (2007).
[18] Y. Hikosaka, P. Lablanquie, F. Penent, T. Kaneyasu, E. Shigemasa, J. H. D. Eland, T. Aoto, and K. Ito, Phys. Rev. A **76**, 032708 (2007).
[19] U. Becker and D. A. Shirley, in *VUV and Soft X-Ray Photoionization* (Plenum Press, New York, 1996).
[20] C. King, M. Tronc, F. H. Read, and R. C. Bradford, J. Phys. B **10**, 2479 (1977).
[21] H. Aksela, S. Aksela, and H. Pulkkinen, Phys. Rev. A **30**, 2456 (1984).
[22] C. F. Fischer, T. Brage, and P. Jönsson, *Computional Atomic Structure: An MCHF Approach* (Institute of Physics Publishing, Bristol, 1997).
[23] F. A. Parpia, C. F. Fischer, and I. P. Grant, Comput. Phys. Commun. **94**, 249 (1996).
[24] S. Fritzsche, J. Electron Spectrosc. Relat. Phenom **114**, 1155 (2001).
[25] S. Fritzsche, Comput. Phys. Commun. **183**, 1525 (2012).
[26] S. Fritzsche, B. Fricke, and W.-D. Sepp, Phys. Rev. A **45**, 1465 (1992).
[27] V. Schmidt, Z. Phys. D **2**, 275 (1986).
[28] G. B. Armen and F. P. Larkins, J. Phys. B **25**, 931 (1992).
[29] U. Becker, R. Wehlitz, O. Hemmers, B. Langer, and A. Menzel, Phys. Rev. Lett. **63**, 1054 (1989).
[30] M. Pahler, C. D. Caldwell, S. J. Schaphorst, and M. O. Krause, J. Phys. B **26**, 1617 (1993).